

Assessment of Computational Fluid Dynamics and Experimental Data for Shock Boundary-Layer Interactions

James R. DeBonis*

NASA John H. Glenn Research Center at Lewis Field, Cleveland, Ohio 44135

William L. Oberkampf†

WLO Consulting, Austin, Texas 78633

Richard T. Wolf,‡ Paul D. Orkwis,§ and Mark G. Turner¶

University of Cincinnati, Cincinnati, Ohio 45221

Holger Babinsky**

University of Cambridge, Cambridge, England CB2 1PZ, United Kingdom

and

John A. Benek††

U.S. Air Force Research Laboratory, Wright-Patterson Air Force Base, Ohio 45433

DOI: 10.2514/1.J051341

A workshop on the computational fluid dynamics (CFD) prediction of shock boundary-layer interactions (SBLIs) was held at the 48th AIAA Aerospace Sciences Meeting. As part of the workshop, numerous CFD analysts submitted solutions to four experimentally measured SBLIs. This paper describes the assessment of the CFD predictions. The assessment includes an uncertainty analysis of the experimental data, the definition of an error metric, and the application of that metric to the CFD solutions. The CFD solutions provided very similar levels of error and, in general, it was difficult to discern clear trends in the data. For the Reynolds-averaged Navier-Stokes (RANS) methods, the choice of turbulence model appeared to be the largest factor in solution accuracy. Scale-resolving methods, such as large-eddy simulation (LES), hybrid RANS/LES, and direct numerical simulation, produced error levels similar to RANS methods but provided superior predictions of normal stresses.

Nomenclature

$E(f)$	= error metric of f
$e(f)_n$	= local error in f
M_∞	= freestream Mach number
p_0	= stagnation pressure
Re_θ	= Reynolds number based on momentum thickness
T_0	= stagnation temperature
U_∞	= freestream velocity
u, v, w	= streamwise, transverse, and spanwise velocity components
$\langle u^2 \rangle$	= streamwise specific normal stress
$\langle v^2 \rangle$	= transverse specific normal stress
$\langle u'v' \rangle$	= specific shear stress
x, y, z	= Cartesian coordinates

$\Delta x, \Delta y,$	= spacing of particle image velocimetry measurement grid
δ	= boundary-layer thickness
θ	= shock deflection angle

subscripts

cfd	= computational fluid dynamics obtained quantity
exp	= experimentally obtained quantity

I. Introduction

A SHOCK boundary-layer interaction (SBLI) is an important and complex fluid dynamic phenomena that occurs in supersonic flows. It is one of the primary flow features in supersonic inlets, and, if not controlled, it can have a major impact on inlet performance. Predicting SBLIs and understanding how to control them is a critical technology area for the development of propulsion systems for supersonic vehicles. The SBLI considered in this study consists of an oblique shock wave impinging on a turbulent wall boundary layer. The shock wave imposes an abrupt adverse pressure gradient that negatively affects the boundary layer, thickening the layer, and perhaps causing separation. The interaction increases turbulence levels in the boundary layer and typically induces unsteadiness in the shock wave. In ducts with rectangular cross sections, the shock also affects the sidewall boundary layer and corner flows, resulting in extremely complex three-dimensional flowfields. An excellent description of the phenomena is given by Delery and Marvin [1]. The phenomena is complex and difficult to predict using computational fluid dynamics (CFD), and it is now generally accepted that analysis must be done in three dimensions to capture the physics of the flowfield. Traditionally, Reynolds-averaged Navier-Stokes (RANS) CFD methods have been used for SBLI predictions. RANS turbulence models are developed and adapted for well-behaved boundary layers and shear layers, and it is not clear if they can accurately model the complex flow in a SBLI. Scale-resolving methods, which include direct numerical simulation (DNS), large-eddy simulation (LES),

Presented as Paper 2010-4823 at the 28th AIAA Applied Aerodynamics Conference, Chicago, IL, 28 June–1 July 2010; received 15 April 2011; revision received 2 September 2011; accepted for publication 13 September 2011. This material is declared a work of the U.S. Government and is not subject to copyright protection in the United States. Copies of this paper may be made for personal or internal use, on condition that the copier pay the \$10.00 per-copy fee to the Copyright Clearance Center, Inc., 222 Rosewood Drive, Danvers, MA 01923; include the code 0001-1452/12 and \$10.00 in correspondence with the CCC.

*Aerospace Engineer, Inlet & Nozzle Branch; james.r.debonis@nasa.gov. Associate Fellow AIAA (Corresponding Author).

†Consulting Engineer; wloconsulting@gmail.com. Fellow AIAA.

‡Undergraduate Researcher, Department of Aerospace Engineering; wolfrt@mail.uc.edu. Student Member AIAA.

§Professor, Department of Aerospace Engineering; orkwispd@ucmail.uc.edu. Associate Fellow AIAA.

¶Associate Professor, Department of Aerospace Engineering; turnermr@ucmail.uc.edu. Associate Fellow AIAA.

**Professor of Aerodynamics, Department of Engineering; hb@eng.cam.ac.uk. Associate Fellow AIAA.

††Director, Computational Sciences Center, Air Vehicles Directorate; john.benek@wpafb.af.mil. Fellow AIAA.

and hybrid RANS/LES, are techniques that directly compute some or all of the turbulence and offer the promise for improved predictions but are just now becoming a practical option for these types of flows due to the availability of increased computing power.

A workshop on the CFD prediction of shock boundary-layer interactions was organized by the American Institute of Aeronautics and Astronautics (AIAA). The purpose of the workshop was to share prediction methodologies, assess the state of the art in SBLI prediction, and determine the most promising methods. A key component of this effort was to provide an objective assessment of the error for each of the predictions. The workshop was preceded by a solicitation for participants to compute one or more shock boundary-layer interaction test cases using their chosen computational method. Four test cases with extensive experimental data were identified, and the geometry and flow conditions for each were provided to the analysts. The experimental data were also provided for two cases: the cases with the weakest shock interactions. The data was withheld for the two cases with the strongest shock interaction to assess the solutions in a true predictive situation. Before the workshop, the participants submitted their solutions for assessment. The workshop was held at the 48th AIAA Aerospace Sciences Meeting in Orlando, Florida, in January 2010. At the workshop, the experimentalists discussed their measurements, and then, the participants presented their results. A preliminary error assessment, further refined for this paper, was also presented. In addition to the assessment of computations, one of the findings of the workshop was the need for careful evaluation of the experimental uncertainty.

Presentations in a special session at the 28th Applied Aerodynamics Conference in Chicago, Illinois, in June 2010, provided a summary of the workshop findings. An overview of the workshop and a summary of the lessons learned were given by Benek [2] and Benek and Babinsky [3]. An oral presentation summarizing the experiments was given by Dr. Holger Babinsky. An assessment of the CFD results was given by Hirsch [4]. Hirsch's assessment of the CFD results is based on a traditional comparison of CFD and experimental data through comparisons between CFD and experimental velocity profiles and contour plots. The present paper, also presented in Chicago, discusses the error assessment of the CFD predictions for the four SBLI workshop cases using an objective error metric [5]. The assessment includes an evaluation of the experimental uncertainty, the definition of the error metric, the results of the error assessment for each test case, and a discussion of some trends that were identified in the data. The findings of this paper are finally compared with Hirsch's findings.

II. Experimental Data

The experiments that provided data for this study were conducted with the aim of creating CFD validation data sets. One data set used at the workshop was taken at the Institut Universitaire des Systèmes Thermiques Industriels (IUSTI) in Marseille, France [6]. Three other data sets were taken at the University of Michigan (UMich.) [7,8].

This paper provides a detailed look at uncertainty in the UMich. data, putting this data under more scrutiny than most other particle image velocimetry (PIV) data. The uncertainty analysis method used here has been applied to other experimental data used for validation of CFD [9–11]. The procedure allows one to quantify the errors when CFD is then compared with the experiments.

The general setup of the experiment was similar for both data sets (Fig. 1). A shock generator plate was placed in the test section of a supersonic wind tunnel at an angle to the freestream flow. This angle, θ , is the shock deflection angle, which determines the strength of the oblique shock wave. A turbulent boundary layer is present on the floor of the wind tunnel. An oblique shock wave is formed by the plate and intersects the boundary layer. PIV measurements of velocities and turbulent quantities were performed in the region of the SBLI. The use of PIV, a relatively new technique, for comparison with CFD represents an advance in the assessment of CFD for SBLIs. Typically, wall pressure and skin friction data have been used. PIV provides a much more detailed look at the flow. Table 1 summarizes the experimental cases. The geometries for both test setups were

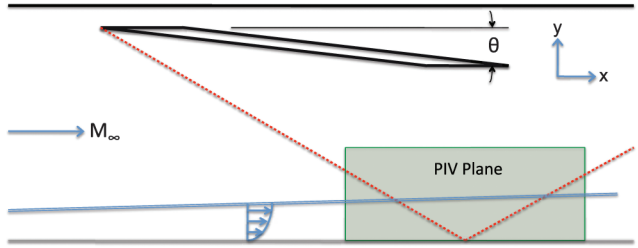


Fig. 1 Schematic of a SBLI in a supersonic wind tunnel.

provided in Initial Graphics Exchange Specification format. The basic layouts of the tunnels, shock generator plates, and cross sections are shown in Fig. 2. The two experimental data sets are summarized in the next subsections. Details of the PIV measurements and their effect on the experimental uncertainty are given in Sec. III.

A. IUSTI Mach 2.25–8.0 Deg Case

The first data set was taken at IUSTI in Marseille, France [6]. The data included two-dimensional PIV, stereoscopic PIV, laser doppler velocimetry (LDV), and wall pressures. The data used here for comparison are the PIV data on a streamwise plane (a plane parallel to the freestream flow and the tunnel sidewall) in the center of the tunnel. The PIV plane was limited to only the interaction region. The LDV measurements were used to verify the PIV data. The data provided for comparison included streamwise and transverse velocities, u and v ; normal stresses, $\sqrt{\langle u^2 \rangle}$ and $\sqrt{\langle v^2 \rangle}$; and shear stress, $-\langle u'v' \rangle$.

B. UMich. Mach 2.75–7.75, 10.0, and 12.0 Deg Cases

The remaining data sets were taken at UMich. [7,8]. The data consists of stereo-PIV measurements on a streamwise plane in the center of the tunnel and several spanwise planes (Fig. 3). The PIV planes include the interaction region and a portion of the freestream flow above. In addition, a spanwise data plane was provided to characterize the boundary layer upstream of the interaction. Lapsa [7] has shown that, at this upstream plane, the wake parameter does not match that of a classical fully turbulent flat plate boundary layer and that difference is caused by the pressure gradient experienced in the wind tunnel nozzle. The data provided included streamwise, transverse, and spanwise velocities, u , v , and w ; normal stresses, $\langle u^2 \rangle$, $\langle v^2 \rangle$, and $\langle w^2 \rangle$; shear stresses, $\langle u'v' \rangle$, $\langle u'w' \rangle$, and $\langle v'w' \rangle$; and velocity gradients. Note that there is a difference between the two experiments in the form of the turbulent stresses.

III. Experimental Uncertainty Estimation

This section discusses how uncertainties in the experimental measurements were estimated. For the IUSTI experiment, an estimate of the experimental uncertainty was obtained from Dussauge et al. [12], and, for the UMich. experiment, an estimate of uncertainty was obtained from Lapsa [7] and Lapsa and Dahm [8]. An independent method to estimate experimental uncertainty developed by Oberkampf and Aeschliman [9], Oberkampf et al. [10], and Oberkampf and Roy [11] was also applied to the UMich. data. The method is based entirely on statistically analyzing the differences in multiple measurements of the various quantities of interest, e.g., u , v , and w , as well as normal and shear stresses.

Table 1 Summary of the experimental cases

Organization	M_∞	U_∞ , m/s	θ , deg	T_0 , K	p_0 , kPa	Re_θ
IUSTI	2.25	544	8.0	293	50.5	6900 Open
UMich.	2.75	603	7.75	293	101	6600 Open
UMich	2.75	603	10.0	293	101	6600 Blind
UMich	2.75	603	12.0	293	101	6600 Blind

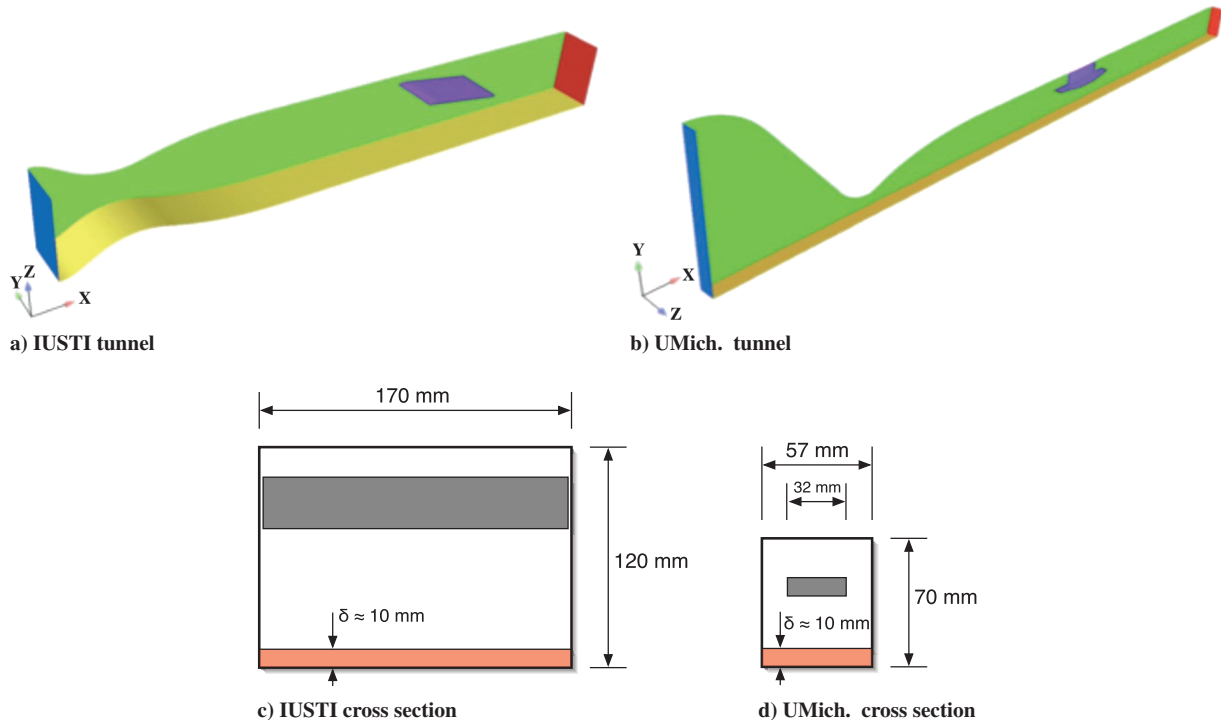


Fig. 2 Wind tunnel and shock generator layout (Figs 2a and 2b courtesy of Vishal Bhagwandin, Army Research Laboratory).

An important issue that was not addressed in either experiment is geometric uncertainty. Differences between the experimental hardware tested and the geometries supplied to the analysts, due to manufacturing or installation errors, are not quantified.

A. IUSTI Data Uncertainty

Spatial resolution of the stereoscopic PIV technique is limited by the thickness of the laser lightsheet (1 mm) and the size of the analysis windows. The final effective cell size is 16 (horizontal) \times 8 (vertical) pixels, leading to the data being averaged over a volume of 1 mm \times 0.5 mm and a light sheet thickness of 1 mm. No detailed analysis of the uncertainty in the velocity measurements was provided, but the estimated uncertainty was quoted as 6 m/s [6]. This value of uncertainty was used in the comparisons of CFD results with IUSTI measurements.

An independent assessment of the accuracy of the PIV measurements was obtained by a number of comparisons with LDV

measurements for the same conditions in the wind tunnel. Good agreement was found between PIV and LDV measurements for both mean velocities as well as turbulent stresses.

B. UMich. Data Uncertainty

The parameters for the PIV setup at UMich. were similar to those used in the IUSTI experiments, except that data were obtained by stereoscopic PIV along a streamwise plane as well as seven spanwise planes, as seen in Fig. 3. The streamwise field of view covers a significantly larger region than each spanwise slice, and, for this reason, the PIV window size and operating parameters differ. In the streamwise plane, a window of 32 \times 32 pixels (the smallest used in the analysis) was approximately equivalent to 1 mm \times 1 mm window size, and the lightsheet thickness was 0.5 mm. A delay of about 1 μ s was set between the two laser pulses. Spanwise planes use a smaller field of view to obtain better spatial resolution, and, as a result, window sizes were 0.5 mm \times 0.5 mm, and the time increment between two laser pulses was around 500 ns.

Although experimental repeatability and statistical uncertainties of the turbulence quantities were computed by the original researchers, no comprehensive uncertainty analysis was provided for the measurements, nor were the PIV measurements compared with an independent technique. However, the repeatability of the measurements was assessed by comparing the results of different test campaigns performed several weeks apart. The different test campaigns involved completely independent forming and positioning of the laser sheets, positioning of the stereo cameras, calibration of the camera fields-of-view, and all other aspects associated with setup and calibration of the experiment. Comparison of the two results through the boundary layer showed that the mean u component of velocity was indiscernible between the two campaigns, except for the first three points near the wall. Comparisons for the mean v component of velocity showed a maximum difference of 9 m/s and the average difference through the boundary layer of 3 m/s.

Several CFD analysts participating in the workshop noticed a discrepancy in the PIV data where the two measurement planes intersect. Discrepancies between two independent measurements is not unexpected and could be attributed to numerous sources, including the difference in in-plane vs out-of-plane measurements,

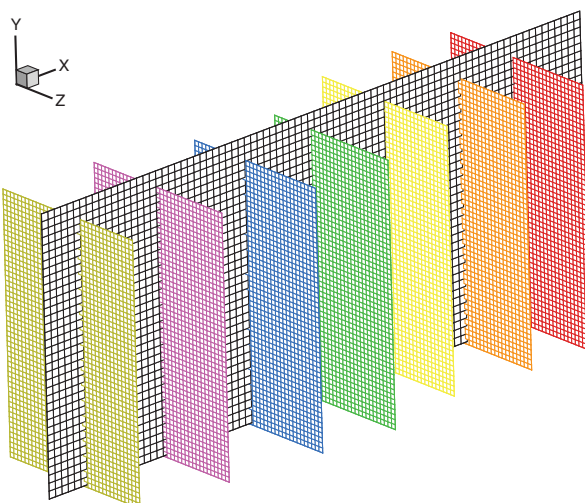


Fig. 3 Streamwise and spanwise planes for PIV measurements for the UMich. data.

window size, or delay time. In the next section, we use these two independent measurements to quantify the uncertainty in the data.

C. Statistical Estimation Method

We took advantage of the fact that the UMich. measurements were made on two different but overlapping planes to apply a completely different approach for estimating the experimental uncertainty. Oberkampf and Aeschliman [9], Oberkampf et al. [10], and Oberkampf and Roy [11] developed this method for estimating experimental uncertainty of measurements obtained in wind tunnels. This technique is a statistical approach based on analyzing comparisons of multiple measurements. It is usually referred to as statistical design of experiments because it analyzes the final measured result of the quantities of interest, based on specially designed sampling techniques [13,14]. Next, a brief description of the approach is given; then, the key computational steps and the results of the analysis are discussed.

The approach compares measurements obtained on both the streamwise and spanwise planes. The quantities of interest can be either directly measured quantities, i.e., mean velocity components u , v , w , and u' , v' , w' , or derived quantities, such as gradients or Reynolds stresses. The uncertainties were estimated at all seven intersections of the spanwise and streamwise planes for the three shock generator angles.

This statistical approach could also be applied to comparisons between multiple measurements of the same quantity in the same plane. This calculation would independently estimate the repeatability uncertainty that was discussed in Sec. III.B. It is well known that this type of repeatability uncertainty, also referred to as 0th order replication [15], is smaller, sometimes much smaller, than the total uncertainty due to other sources in an experiment.

When comparisons are made between multiple measurements of the same quantity in different planes, then, in addition to the

repeatability uncertainty just mentioned, one can capture a wider range of systematic (bias) uncertainties. Examples of these systematic uncertainties are any changes in the calibration procedure of the PIV system (such as spatial positioning of the laser sheet or measurement volume), changes in the optical setup of the laser sheet used in the PIV system, and changes in PIV window size or spatial resolution. The effect of these types of systematic uncertainties can be quantified by using streamwise and spanwise measurements because, now, correlated bias uncertainties arising from different populations have been sampled. That is, anytime a quantity of interest can be measured and some source of uncertainty can be altered, a modified population is sampled. The more independent each modified population is, the more accurate the estimate of the true (total) uncertainty. For example, improvement to the uncertainty estimate can be obtained by using additional velocity measurements like LDV or hot wire anemometry or by performing measurements in a separate wind tunnel facility.

One must interpolate both planes of data to common points in space to compare quantities of interest at the intersection of two planes. Bilinear interpolation in each plane of data was used to obtain each quantity of interest at the intersection points; x is defined by the x value of the spanwise data plane, y is defined by the y value of the streamwise data plane, and z is defined by $z = 0$ (the z coordinate of the streamwise data plane). The spacing of the measurement points was $\Delta x = \Delta y = 0.5024$ mm and $\Delta y = \Delta z = 0.2879$ mm in the streamwise and spanwise planes, respectively. As a result, the bilinear interpolation of the measurements required no more than half the appropriate distance for the interpolation.

Figure 4 shows the residuals of the u , v , and w mean velocity components for the 21 streamwise and spanwise plane intersections (seven spanwise plane intersections for each of the three shock generator angles). Each intersection has 30–35 measurement points in the streamwise plane, yielding a total 681 residuals for each quantity. Each residual in Fig. 4 is the difference between the

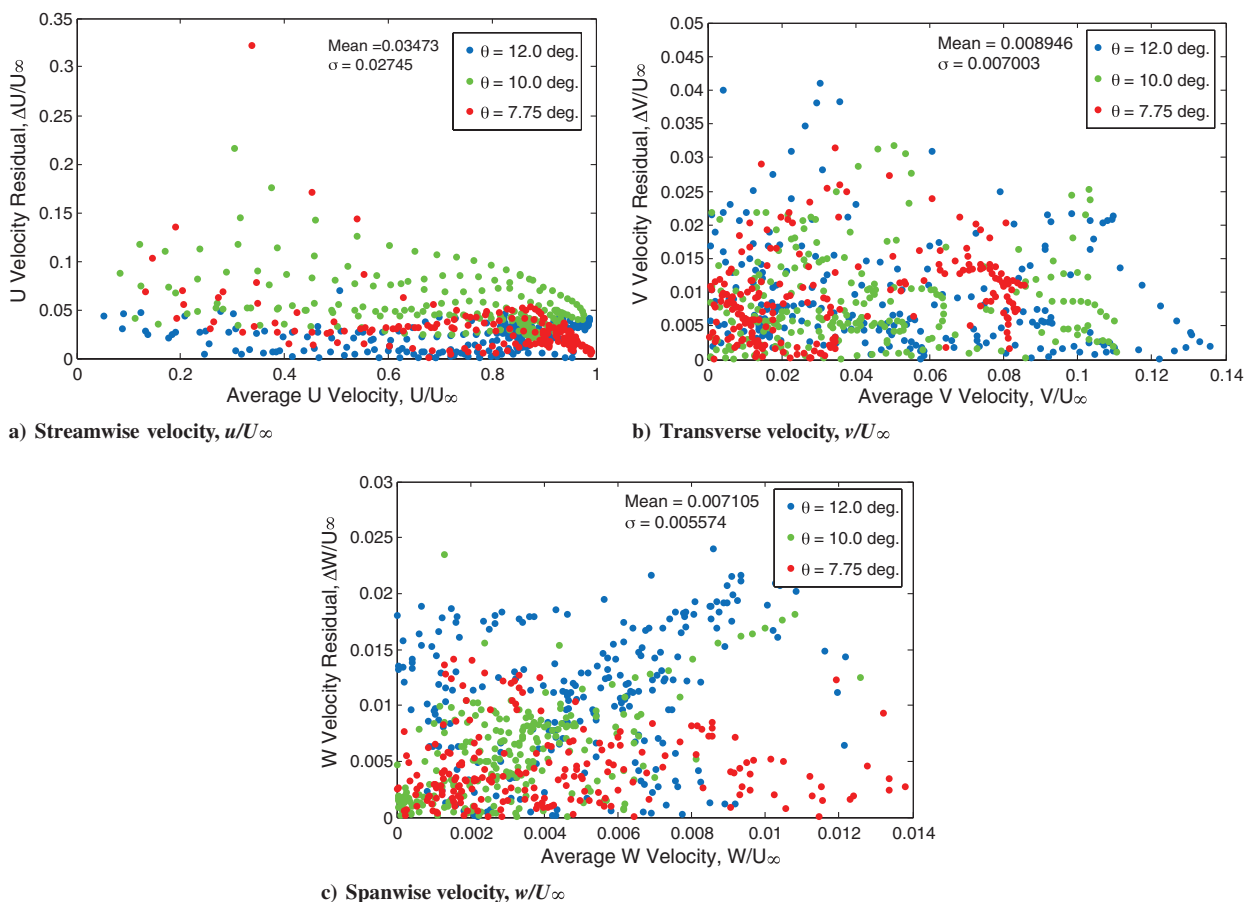


Fig. 4 Residuals of multiple measurements of velocity vs mean velocity components from the UMich. experiment.

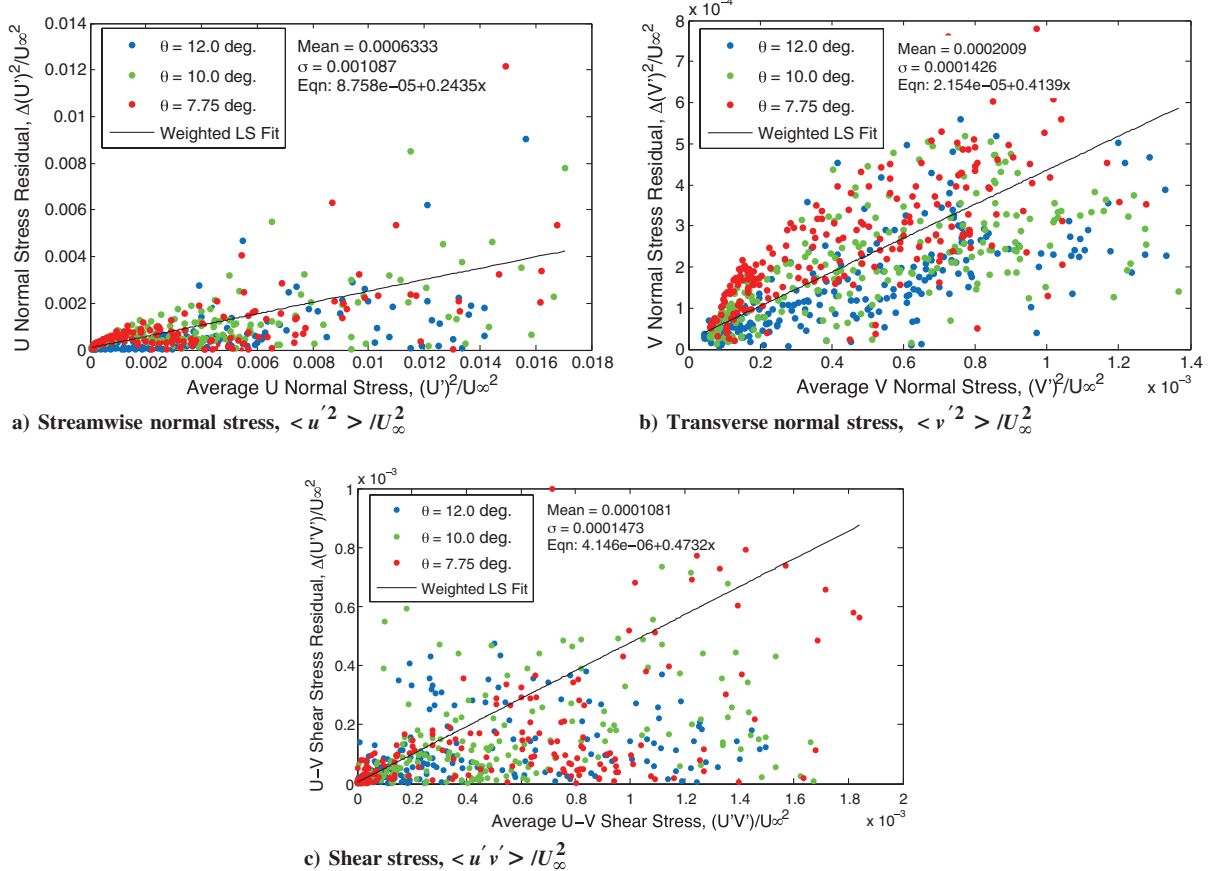


Fig. 5 Residuals of turbulent stresses vs the average stress in each plane from the UMich. experiment.

measurement in each plane, and this is plotted against the average value of the quantity in both planes. None of the scatter plots show a clear trend with residual changes as a function of velocity magnitude or variation of the deflection angle.

Also shown in each figure is the mean and standard deviation of the nondimensional residuals. As can be seen, the mean of the u residuals is about four times larger than the mean of v and w . The non-dimensional mean uncertainty for v and w are seen to be very similar. Converting these means to dimensional quantities, the mean u , v , and w uncertainty was found to be 21 m/s, 5.0 m/s, and 4.0 m/s, respectively. As expected, the statistical uncertainty in u is larger than the uncertainty in v because of two reasons: 1) u is a factor of 10 larger than v and 2) u is the velocity component that is normal to the spanwise plane. It is well known in stereo-PIV measurements that the uncertainty of the velocity component normal to the measurement plane is typically two to three times larger than the velocity components measured in the plane. The mean uncertainty for v is about twice the estimate of the repeatability uncertainty quoted in Sec. III.B. Note that, even though the w velocity component is normal to the streamwise plane, its mean uncertainty is slightly smaller than the v component. The v component is the only component that occurs in both the streamwise and spanwise planes, and, as a result, it would be expected that the mean uncertainty would be smaller than that in w .

A similar set of residual plots was generated for each quantity. Here, only three sample results are shown. Figure 5a shows the

residuals of the streamwise normal stress $\langle u'^2 \rangle / U_\infty^2$ vs the average normal stress at the intersection of the planes. Here, an increase in uncertainty as a function of the magnitude of the stress is observed. This type of scatter plot for uncertainty can be represented by a linear regression function and a normally distributed random error component. Figure 5b shows the residuals of the transverse normal stress $\langle v'^2 \rangle / U_\infty^2$ vs the magnitude of its average values in each plane. Figure 5c shows $\langle u'v' \rangle / U_\infty^2$ vs the average of $\langle u'v' \rangle / U_\infty^2$ in each plane. For other quantities, the plots of the residuals are similar to $\langle u'^2 \rangle / U_\infty^2$. The linear regression indicates that the uncertainties in the Reynolds stresses increase with their magnitude. The slope gives an indication of relative magnitude of the uncertainty with respect to the value of the quantity and can be converted into a percentage. We see, then, that this indicates the uncertainty in $\langle u'^2 \rangle / U_\infty^2$ relative to its magnitude is 24%; for $\langle v'^2 \rangle / U_\infty^2$, it is 44%, and, for $\langle u'v' \rangle / U_\infty^2$, it is 47%. The magnitude of these uncertainties is important in attempting to assess the accuracy of CFD simulations.

The linear variation in the uncertainty of the Reynolds stresses is clear from the statistical analysis; however, the authors do not fully understand the reason for this trend. One possible explanation is that the UMich. streamwise planes may have insufficient PIV data samples for low frequency turbulent structures. It is noted that only 500 samples were taken in this case, whereas 3000 samples were taken for the IUSTI data. The argument, then, is that low sampling rates might underrepresent low frequency events associated with large-scale turbulence structures, whereas they are sufficient for

Table 2 Summary of the statistical uncertainty analysis

	u/U_∞	v/U_∞	w/U_∞	$\langle u'^2 \rangle / U_\infty^2$	$\langle v'^2 \rangle / U_\infty^2$	$\langle u'v' \rangle / U_\infty^2$
Mean uncertainty	0.03473	0.008946	0.007105	$6.333 \cdot 10^{-4}$	$2.009 \cdot 10^{-4}$	$1.081 \cdot 10^{-4}$
Standard deviation of the uncertainty	0.02745	0.007003	0.005574	0.001087	$1.426 \cdot 10^{-4}$	$1.473 \cdot 10^{-4}$
Linear regression slope, a				0.2435	0.4139	0.4732
Linear regression intercept, b				$8.758 \cdot 10^{-5}$	$2.154 \cdot 10^{-5}$	$4.146 \cdot 10^{-6}$

Table 3 Summary of the submitted solutions

Name	Organization	Code	Method	Turbulence Model
Baurle	NASA Langley	Vulcan	RANS	Menter BSL [16]
Baurle	NASA Langley	Vulcan	RANS	Menter SST [16]
Baurle	NASA Langley	Vulcan	RANS	Wilcox $k-\omega$ [17]
Baurle	NASA Langley	Vulcan	RANS	Wilcox $k-\omega$ + Durbin correction [18]
Bhagwandin	Army Research Lab	CFD++	RANS	Realizable $k-e$ [19]
Bhagwandin	Army Research Lab	CFD++	RANS	Spalart-Allmaras [20]
Bhagwandin	Army Research Lab	CFD++	RANS	Menter SST
Duraisamy	Stanford Univ.	Joe	RANS	Menter SST
Edwards	North Carolina State Univ.		RANS/LES	Gieseking et al. [21]
Edwards	North Carolina State Univ.		RANS	Menter SST
Georgiadis	NASA Glenn	Wind-US	RANS	Menter SST
Jamalamadaka	Michigan State Univ.		LES	MKEV [22]
Park [23]	NASA Langley	FUN3D	RANS	Spalart-Allmaras
Pirozzoli [24]	Univ. Roma		DNS	Reduced $Re_\theta = 3725$
Rumsey	NASA Langley	CFL3D	RANS	Spalart-Allmaras
Subbareddy	Univ. of Minnesota	US3D	RANS/LES	IDDES [25]
Tapee	Northrup-Grumman		RANS	Proprietary

higher frequency, small-scale structures. This supposition cannot be tested in the current work but is suggested as an area of concern for future CFD validation experiments.

Table 2 summarizes the results of the statistical uncertainty estimation for a number of quantities of interest. For all quantities of interest, the table shows values for the mean and standard deviation of the residuals. For quantities that show a linearly increasing trend of the uncertainty, the table also shows the value of the slope and intercept of the linear regression ($Y = aX + b$).

IV. CFD Solutions

Eleven individuals from nine different organizations submitted solutions to the workshop for evaluation. Table 3 summarizes the submissions. The solutions were from both RANS methods and scale-resolving Navier-Stokes methods, which includes DNS, LES, and hybrid RANS/LES methods. The RANS methods employed a variety of turbulence models, and the scale-resolving methods used a variety of subgrid models and numerical schemes. Both structured and unstructured grid methods were employed. To encourage participation, the workshop organizers pledged not to associate the submitter's name with individual solutions and error measures. Individual solutions were assigned a letter designation for use in reporting the error metric.

The majority of RANS submissions modeled the entire wind tunnel from the nozzle plenum to downstream of the test section. In these cases, the tunnel stagnation temperature and pressure were specified in the plenum. The scale-resolving calculations typically used a RANS simulation as an initial solution and to provide a mean inflow profile to the unsteady simulation of the test section. The scale-resolving solutions also required a fluctuating component to the inflow profile. This was obtained through boundary-layer recycling techniques, precursor simulations, or theoretical means.

All of the analysts were responsible for post-processing their solutions. This included interpolating their solutions onto the experimental measurement grids and ensuring that the quantities were provided in the proper dimensional form. The analysts were free to choose which cases to run and what data to provide. A total of 36 solutions were provided, and 21 included the turbulent stresses.

A. Description of the Error Metric

An error metric, $E(f)$, was defined to objectively evaluate the submitted solutions. First, we define the local error as the magnitude of the difference between the CFD and experiment:

$$e(f)_n = |(f_{\text{cf}})_n - (f_{\text{exp}})_n| \quad (1)$$

The validation metric is defined as the average of this error over the measurement plane:

$$E(f) = \frac{1}{N} \sum_{n=1}^N e(f)_n \quad (2)$$

For the error in velocities, the metric is nondimensionalized by the freestream velocity, U_∞ . For the error in the turbulence shear stress, the metric is nondimensionalized by the square of the freestream velocity, U_∞^2 . The IUSTI normal stresses ($\sqrt{\langle u^2 \rangle}$ and $\sqrt{\langle v^2 \rangle}$) are nondimensionalized by U_∞ , and the UMich. normal stresses ($\langle u^2 \rangle$ and $\langle v^2 \rangle$) are nondimensionalized by U_∞^2 . The error metric, $E(f)$, has been chosen specifically to compare the CFD solutions with the experiment. It is an average over the experimental window. The errors are relatively small away from the shock and boundary layer, so the size of this experimental window would change the value of the error metric $E(f)$. For a detailed discussion of the construction and use of validation metrics, see Oberkampf and Roy [11].

B. Examination of Representative Solutions

The error metric was computed for all of the variables and all of the solutions. In the interest of brevity, the comparisons shown here are limited to streamwise and transverse velocities, as well as Reynolds turbulent stresses. Only the streamwise measurement plane is shown for the UMich. cases. The velocity derivatives from the UMich. experiment were computed using the experimentally obtained velocities and differenced on the PIV measurement grid. They do not provide any additional information for comparison beyond the velocity data and are a poor comparison to the CFD because the latter were computed on their own much finer grids. The spanwise velocity, w/U_∞ , is also a poor quantity for comparison to CFD on the centerline. The tunnel geometry is symmetric about this plane. The experimental data reveals that the spanwise velocity was not zero, indicating asymmetry in the flow or some instrumentation bias. CFD cannot reliably predict such asymmetries and, in almost all cases, will produce symmetric solutions (in many cases, symmetry was specified in the computation) with zero spanwise velocity.

Because the streamwise velocity, u/U_∞ , is the dominant component, it is the primary focus of our attention. First, the general characteristics of the flowfields and the error metrics will be presented. For each case, the solutions with the lowest (best) and highest (worst) measure of error in streamwise velocity, $E(u)/U_\infty$, will be shown.

1. IUSTI Mach 2.25–8.0 Deg Case

Figure 6 compares contours of streamwise velocity for the experiment and the best and worst CFD predictions of the IUSTI Mach 2.25, $\theta = 8.0$ deg case. For this case, the measurement plane extends vertically only to the edge of the interaction. The shock wave is not visible. The flow separates from the wall, and the boundary layer downstream of the separation bubble is significantly thicker.

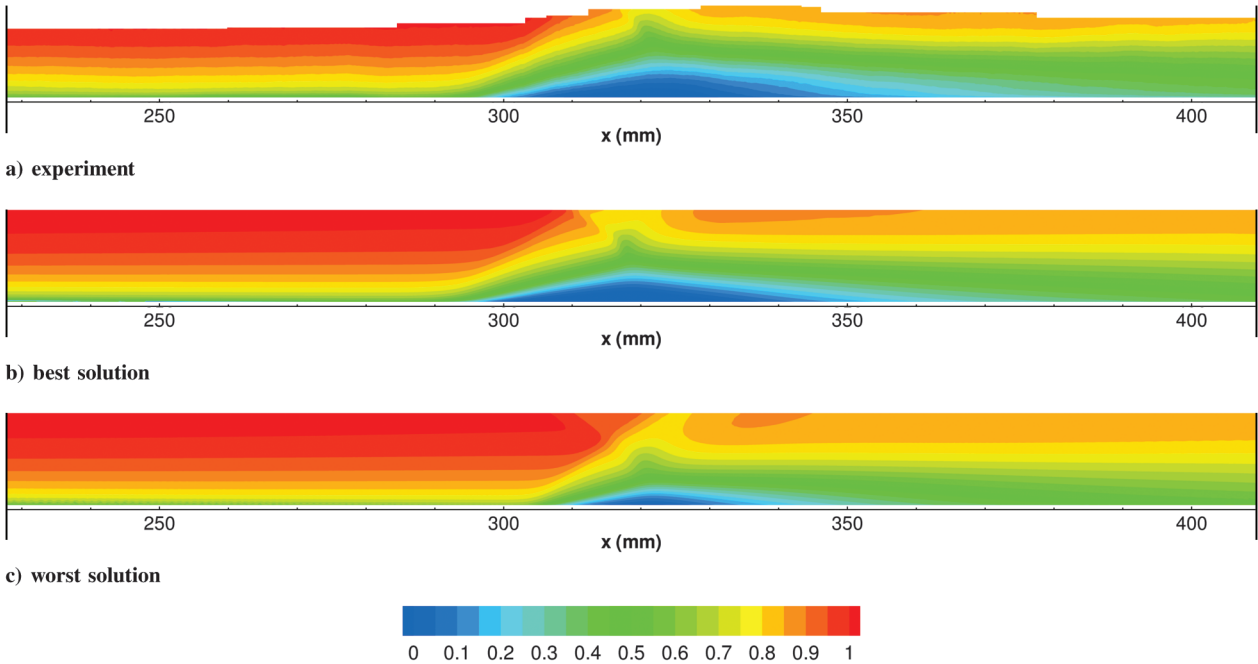


Fig. 6 IUSTI $M = 2.25$ $\theta = 8.0$ deg, contours of streamwise velocity, u/U_∞ .

The best solution appears very similar to the experiment, although the size of the separation bubble and downstream boundary layer are slightly underpredicted. This solution was obtained with a RANS code, using the Spalart-Allmaras (SA) turbulence model [20]. The worst solution shows a much smaller separation and thinner downstream boundary layer. This solution was obtained with a $k-\epsilon$ turbulence model (for an example, see Launder and Sharma [26]), which is well known for the underprediction of the size of separation bubbles. Other solutions using the same grid and code but with different turbulence models showed better agreement. Figure 7 shows the contours of the error for the streamwise velocity. The contours clearly show the regions where the predictions deviate from the PIV data. The regions of high error are concentrated near the separation bubble. The maximum error in the best solution is approximately $0.2U_\infty$, whereas the maximum error in the worst solution is near $0.35U_\infty$. A more traditional comparison is shown in Fig. 8, where velocity profiles are given at several streamwise locations. Error bars based on the experimentalists' estimate [6] are included on the PIV data but are within the size of the symbols representing the data. Despite the fact that the PIV method cannot measure very near the wall, it seems apparent from the profiles that the best solution should do a much better job of predicting quantities of interest, such as skin friction.

2. UMich. Mach 2.75–7.75, 10.0, and 12.0 Deg Cases

Figure 9 compares contours of streamwise velocity for the experiment and the best and worst CFD predictions of the UMich. Mach 2.75 $\theta = 10.0$ deg case. For the UMich. cases, the measurement plane extends beyond the interaction to include a portion of the freestream flow. The shock wave is visible but appears to be smeared in the data. This smearing could be due to some unsteadiness in the shock position and/or the volume-averaging nature of the PIV technique. Figure 10 shows the contours of the error for the streamwise velocity. In addition to the error in the interaction region, the plots show some error in the location of the shock wave and its reflection. Velocity profiles are shown in Fig. 11. Error bars based on the analysis in this paper are included on the PIV data. Although not shown, plots for the UMich. $\theta = 7.75$ deg and $\theta = 12.0$ deg are very similar. As the deflection angle increases, the interaction grows larger. For the 10 deg and 12 deg cases, the boundary layer may be separated. The experimental data is not close enough to the wall to capture any reverse flow, but one could infer it from the boundary-layer profiles. The error in the CFD predictions increases as the shock angle increases. For the $\theta = 7.75$ deg case, both the best and worst solutions were obtained using hybrid RANS/LES techniques. They underpredict the size of the interaction region and downstream boundary-layer thickness. For the $\theta = 10.0$ deg and $\theta = 12.0$ deg

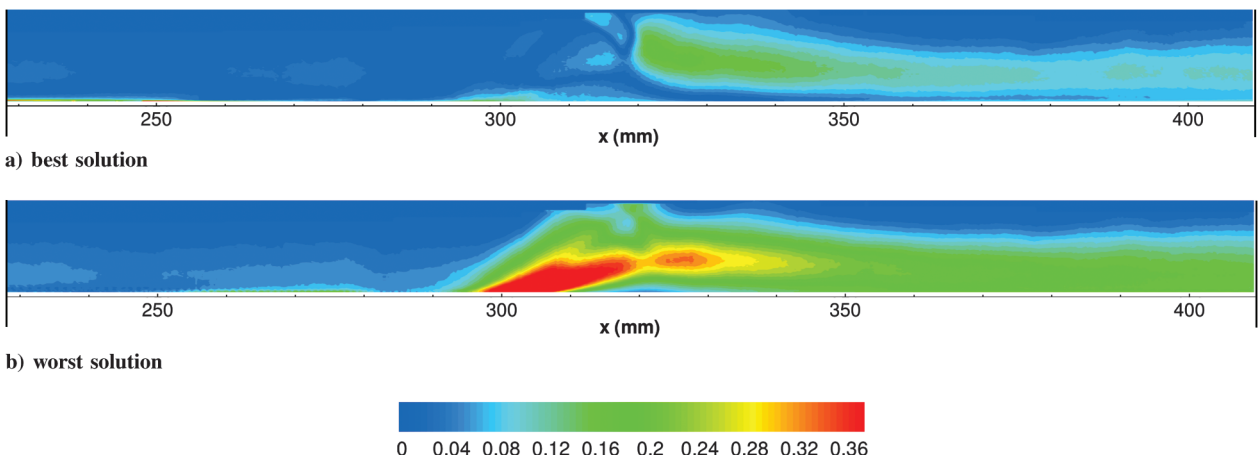


Fig. 7 IUSTI $M = 2.25$ $\theta = 8.0$ deg, contours of streamwise velocity error, $e(u)/U_\infty$.

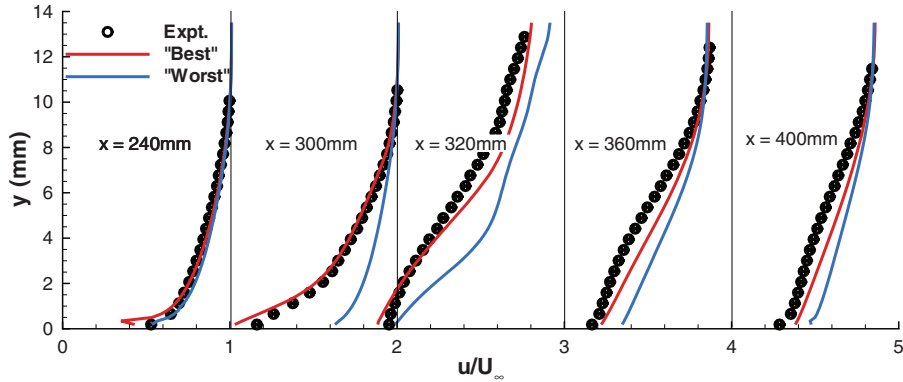


Fig. 8 IUSTI $M = 2.25 \theta = 8.0$ deg, streamwise velocity profiles, u/U_∞ .

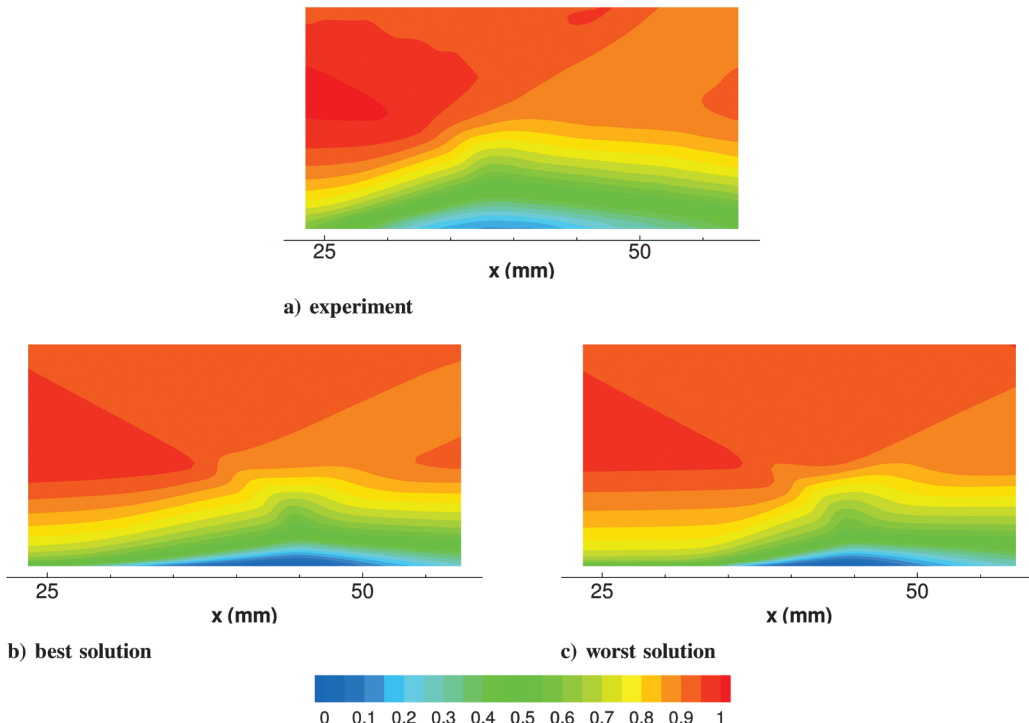


Fig. 9 UMich. $M = 2.75 \theta = 10.0$ deg, contours of streamwise velocity, u/U_∞ .

cases, the best and worst solutions were provided by the same researcher on the same grid but by using different turbulence models, indicating the strong dependence on model choice. The effect of turbulence modeling is further discussed in Sec. IV.E.1.

C. Prediction of Turbulent Stresses

The turbulent stresses are computed very differently, depending on the numerical approach used. For the RANS solutions submitted, the stresses are not explicitly computed and must be derived from the

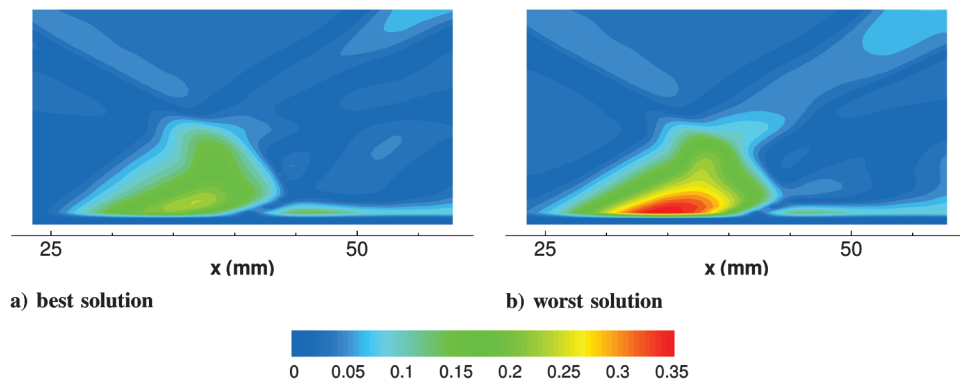


Fig. 10 UMich. $M = 2.75 \theta = 10.0$ deg, contours of streamwise velocity error, $e(u)/U_\infty$.

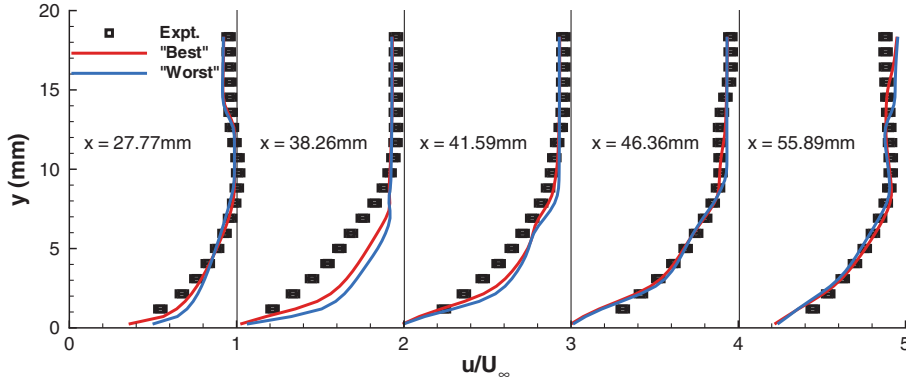


Fig. 11 UMich. $M = 2.75$ $\theta = 10.0$ deg, streamwise velocity profiles, u/u_∞ .

turbulence model variables. Typically, the Boussinesq approximation is used to compute the components of the stress tensor based on the turbulent kinetic energy from a two-equation model. In the case of a one-equation turbulence model, an additional approximation for turbulent kinetic energy must be made. An example of how this may be done is given by Georgiadis et al. [27]. For the scale-resolving methods, the majority of the turbulent motion is computed directly in the simulation. The exact amount is dependent on the grid resolution and subgrid scale modeling used. Because the scale-resolving solutions have less reliance on modeling approximations, one can expect that they will yield better results.

Two predictions for the turbulent stresses were submitted for the IUSTI case: one RANS and one scale-resolving method. The solutions are compared with the experiment in Figs. 12–14. The experimental data show very high levels of streamwise normal stress in the forward portion of the interaction region. This feature is predicted well by the scale-resolving method and missed by the RANS (Fig. 12).

The experiment shows that the form and levels of the transverse normal stress differ significantly from the streamwise normal stress. The scale-resolving solution depicts this change accurately. The RANS prediction of the two normal stresses are very similar. This deficiency in the RANS prediction is a direct consequence of the approximate method necessary to derive the stresses from the turbulence model.

The shear stress is shown in Fig. 14. Here, the RANS solution is much improved. The improved prediction of the shear stress for

RANS is not surprising. RANS turbulence models directly affect the solution through the shear stress term in the equations, and the models are developed and tuned to accurately model this term. For the scale-resolving solution, the shear stress in the boundary layer upstream of the interaction is poorly predicted. This highlights two current problem areas in scale-resolving methods: the difficulty in predicting near-wall turbulence and the accurate specification of initial boundary-layer conditions. The scale-resolving method does a superior job downstream of the interaction.

D. Comparison of All Solutions

1. IUSTI, Mach 2.25, $\theta = 8.0$ Deg

The error for all seven predictions (denoted A through G) of the IUSTI case are given in Table 4. For the velocity components, the experimental uncertainty quoted by the experimentalists, 1.1% of the freestream velocity, is given in the first line. The average error in streamwise velocity for the CFD predictions ranged between 3.8 and 9.0% of the freestream velocity, which is well above the experimental error. The errors in transverse velocity are all near the experimental uncertainty. The relative accuracy of the methods is not consistent between the variables shown here. For example, submission F provides the lowest error in streamwise velocity, but it provides the highest error in transverse velocity. The error in the prediction of the turbulent stresses corresponds to the discussion in Sec. IV.C. The scale-resolving prediction, D, does a superior job for

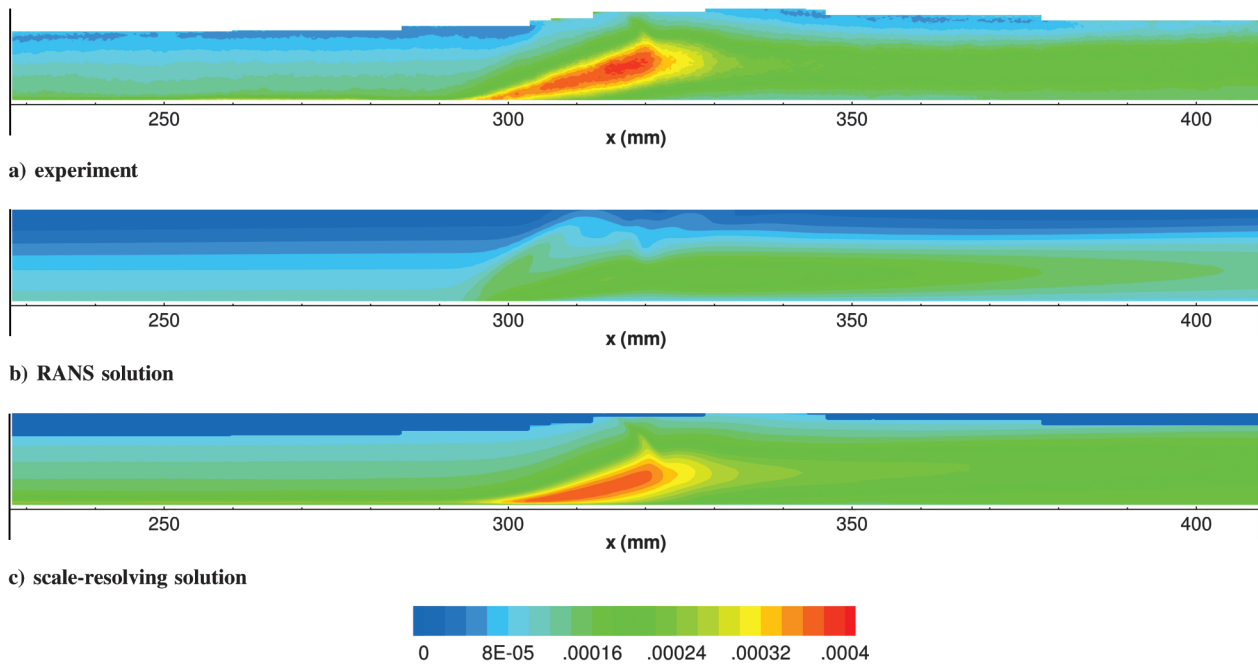


Fig. 12 IUSTI $M = 2.25$ $\theta = 8.0$ deg, contours of streamwise normal stress, $\sqrt{\langle u^2 \rangle} / (U_\infty)^2$.

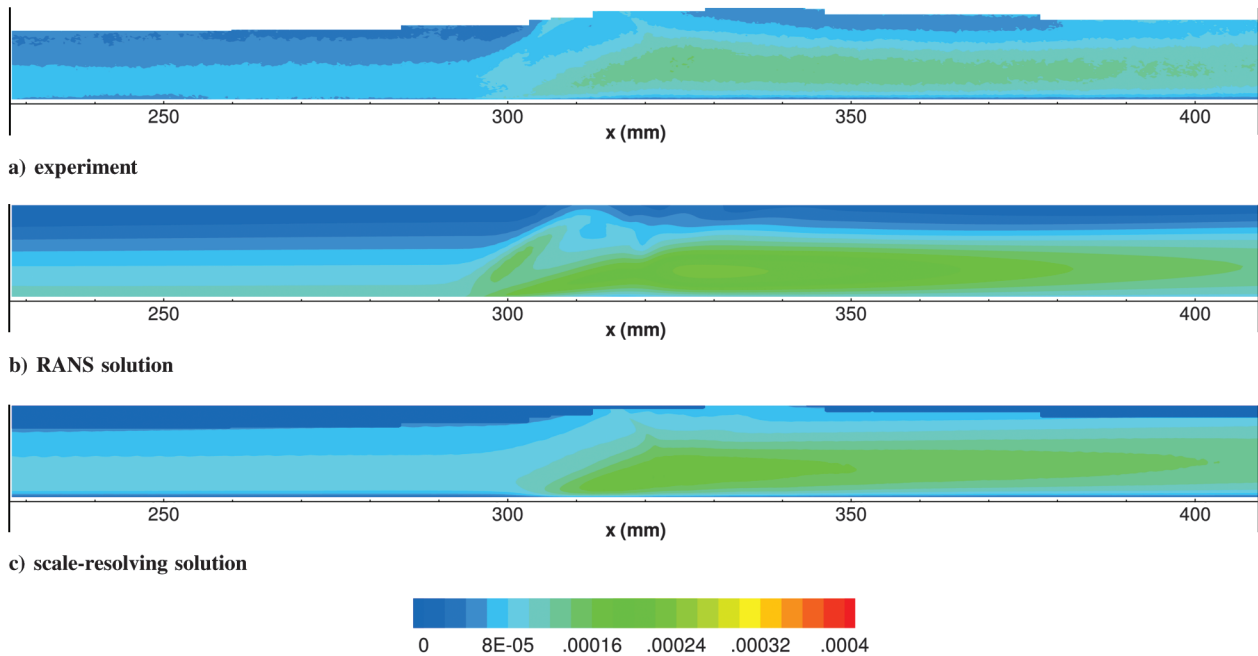


Fig. 13 IUSTI $M = 2.25$ $\theta = 8.0$ deg, contours of transverse normal stress, $\sqrt{\langle v^2 \rangle} / (U_\infty)^2$.

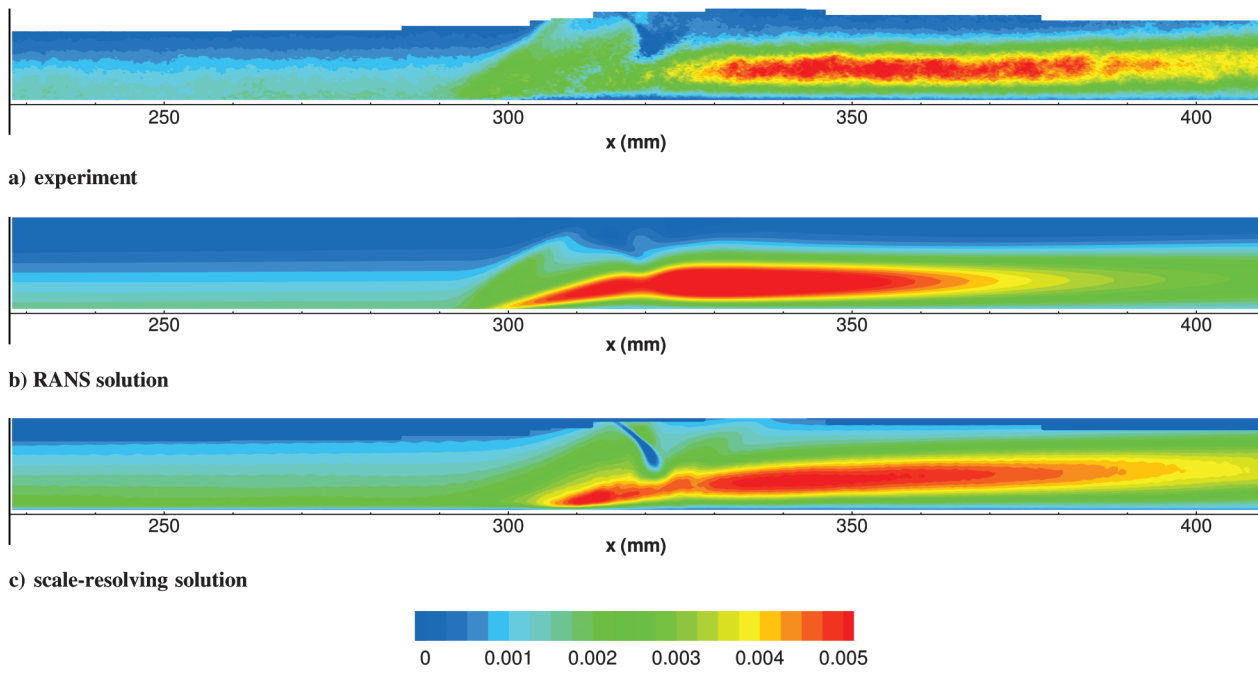


Fig. 14 IUSTI $M = 2.25$ $\theta = 8.0$ deg, contours of shear stress, $-\langle u'v' \rangle / (U_\infty)^2$.

the normal stresses, and the RANS prediction, G, is better for the shear stress.

2. UMich. Mach 2.75–7.75, 10.0, and 12.0 Deg Cases

The errors for all predictions of the UMich., Mach 2.75 cases are given in Tables 5–7. The experimental uncertainties from the statistical estimation are also listed. For the Reynolds stresses, we computed the uncertainty for each plane based on the linear regression, and these values differ from the mean uncertainties for all planes listed in Table 2. All of the CFD predictions of streamwise velocity and streamwise normal stress are near (many are below) the levels of the experimental uncertainty. This suggests that any conclusions based on the error data are not valid. But, as shown in Fig. 11, the predictions lie outside of the experimental error bars in

the interaction region, suggesting that the use of this error metric with the current data can still be useful.

The computed errors in streamwise velocity for the best and worst CFD predictions are given in Table 8. The errors grow with increasing deflection angles. This is expected and is a result of the stronger shock wave, larger interaction region, and more complex flowfield. The lower average errors compared with the IUSTI case are due to the inclusion of a portion of the freestream flow in the plane of interest. The freestream portion of the flow is much better predicted than the interaction region. Including this portion of the flowfield in the error calculation results in a lower average error (Fig. 10). It must also be noted that the data were withheld from the participants for both the 10 deg and 12 deg cases. It is possible that this fact contributed to the larger errors at these shock generator angles.

As with the IUSTI case, there does not appear to be a correlation between prediction methodologies and the relative error for each variable examined.

E. Discussion of Trends in the Data

In general, the errors in the CFD solutions all fell within a relatively narrow band, and no one method predicted all variables well. No method stood out as being clearly superior to the others. However, the error contours and velocity profiles indicate that there is room for improvement in the modeling. RANS methods, such as Reynolds stress and algebraic Reynolds stress models, may offer improved predictions of the turbulent stresses and other flow quantities. Also, the scale-resolving predictions suggest that, as the methods mature, results will improve.

The submitted solutions provided a wealth of information. But, because each analyst used a different approach, there are a large number of variables to consider when attempting to analyze the results. These variables include the numerical scheme, grid resolution, grid type, boundary conditions, turbulence model, gas model, etc. Based on the information that was submitted with the results and presented at the workshop, an attempt was made to discern trends in the error data. This is by no means a complete analysis. And it is suggested that, to do a more thorough study, future efforts should include submitted solutions that employ common elements, such as grids, numerical schemes, etc.

1. Effect of the RANS Turbulence Model

The clearest discernible effect on the solutions for the RANS submissions was that of the turbulence model. There were seven RANS methodologies that were run for all three UMich. flow cases. For the 7.75 deg case, all the Menter shear stress transport (SST),

Wilcox $k-\omega$, and SA model solutions are within 0.5% of each other. At the larger deflection angles, the error in all of the solutions increases, and a clear trend is seen. All of the methods show the same relative error levels for the 10 and 12 deg cases. The Wilcox $k-\omega$ models provide the lowest error, and the Menter baseline (BSL) model has the highest error. The Menter SST and SA models produce similar error levels in between the minimum and maximum levels. For the 7.75 deg case, several models also exhibit the same behavior in the relative error. The error for two Menter SST, the SA, and the Menter BSL predictions behave similarly to the 10 and 12 deg cases. The Wilcox $k-\omega$ and one of the Menter SST predictions do not follow the trend.

A closer examination of the submitted solutions reveals that the predictions are strongly determined by the turbulence model used. This is illustrated by the following criteria:

- 1) The three Menter SST solutions were from different submissions and used different grids and codes, yet there are only slight differences between them; and
- 2) One of the Menter SST solutions, the Wilcox $k-\omega$ solution, and the Menter BSL solution were all obtained using the same grid and code, illustrating a strong dependence on turbulence model.

2. Effect of RANS vs Scale-Resolving Methods

The UMich. Mach 2.75, $\theta = 7.75$ deg case was the only case where multiple scale-resolving solutions were submitted. The scale-resolving solutions were the best and worst predictions for this case. The best and worst RANS and scale-resolving predictions are indicated in Table 5. Both methods produce very similar error levels. But, because RANS methods are far more mature than scale-resolving methods, there is still potential for scale-resolving methods to provide superior predictions. In addition, if the prediction of

Table 4 Error assessment of the IUSTI Mach 2.25, $\theta = 8.0$ deg case

Case	Error in						Turbulence model
	u/U_∞	v/U_∞	$\sqrt{\langle u^2 \rangle}/U_\infty$	$\sqrt{\langle v^2 \rangle}/U_\infty$	$-\langle u'v' \rangle/U_\infty^2$	Grid type	
Experiment.	0.01100	0.01100					
A	0.09014	0.01479				Unstructured	Realizable $k-\epsilon$
B	0.08200	0.01297				Structured	Menter SST
C	0.04839	0.01497				Unstructured	Menter SST
D	0.04227	0.007343	$2.526 \cdot 10^{-5}$	$2.068 \cdot 10^{-5}$	$5.564 \cdot 10^{-4}$	Structured	DNS, reduced Re_θ
E	0.06420	0.01040				Unstructured	Spalart-Allmaras
F	0.03867	0.01847				Unstructured	Spalart-Allmaras
G	0.05180	0.008487	$4.185 \cdot 10^{-5}$	$2.565 \cdot 10^{-5}$	$4.644 \cdot 10^{-4}$	Structured	Spalart-Allmaras

Table 5 Error assessment of the UMich. Mach 2.75, $\theta = 7.75$ deg case

Case	Error in						Turbulence model
	u/U_∞	v/U_∞	$\langle u^2 \rangle/U_\infty^2$	$\langle v^2 \rangle/U_\infty^2$	$\langle u'v' \rangle/U_\infty^2$		
Experiment	0.03473	0.008946	$5.187 \cdot 10^{-4}$	$1.320 \cdot 10^{-4}$	$1.750 \cdot 10^{-4}$		
B ^a	0.02633	0.01449					Menter SST
F	0.02840	0.01729					Spalart-Allmaras
G	0.02759	0.01716	$4.496 \cdot 10^{-4}$	0.001131	$2.676 \cdot 10^{-4}$		Spalart-Allmaras
H ^b	0.03571	0.02721	$7.055 \cdot 10^{-4}$	$8.947 \cdot 10^{-4}$	$2.912 \cdot 10^{-4}$		Menter BSL
I	0.02957	0.04002					Menter SST
J ^c	0.03995	0.02344	$8.536 \cdot 10^{-4}$	$6.702 \cdot 10^{-4}$	$2.639 \cdot 10^{-4}$		RANS/LES
K	0.02999	0.01867					Proprietary
L	0.03980	0.03883					LES
M	0.02899	0.01771	$6.856 \cdot 10^{-4}$	$8.261 \cdot 10^{-4}$	$1.854 \cdot 10^{-4}$		Menter SST
N	0.03035	0.01917	$7.889 \cdot 10^{-4}$	$7.801 \cdot 10^{-4}$	$2.268 \cdot 10^{-4}$		Wilcox $k-\omega$ + Durbin correction
O	0.03129	0.01961	$7.834 \cdot 10^{-4}$	$7.882 \cdot 10^{-4}$	$2.321 \cdot 10^{-4}$		Wilcox $k-\omega$
P	0.02669	0.01682	$7.983 \cdot 10^{-4}$	$7.042 \cdot 10^{-4}$	$1.463 \cdot 10^{-4}$		Menter SST
Q ^d	0.02373	0.01828					RANS/LES

^aBest RANS

^bWorst RANS

^cWorst scale-resolving

^dBest scale-resolving

Table 6 Error assessment of the UMich. Mach 2.75, $\theta = 10.0$ deg case

Case	Error in					Turbulence model
	u/U_∞	v/U_∞	$\langle u^2 \rangle / U_\infty^2$	$\langle v^2 \rangle / U_\infty^2$	$\langle u'v' \rangle / U_\infty^2$	
Experiment	0.03473	0.008946	$6.097 \cdot 10^{-4}$	$1.513 \cdot 10^{-4}$	$1.739 \cdot 10^{-4}$	
B	0.03525	0.02275				Menter SST
G	0.03698	0.02043	$8.992 \cdot 10^{-4}$	0.001217	$3.401 \cdot 10^{-4}$	Spalart-Allmaras
H	0.04584	0.04158	0.001172	0.001121	$4.863 \cdot 10^{-4}$	Menter BSL
I	0.04011	0.03611				Menter SST
M	0.03545	0.02580	$8.940 \cdot 10^{-4}$	$9.218 \cdot 10^{-4}$	$2.612 \cdot 10^{-4}$	Menter SST
N	0.03464	0.02742	0.001058	$9.305 \cdot 10^{-4}$	$3.405 \cdot 10^{-4}$	Wilcox $k-\omega$ + Durbin correction
O	0.03368	0.02664	0.001054	$9.276 \cdot 10^{-4}$	$3.377 \cdot 10^{-4}$	Wilcox $k-\omega$
P	0.03742	0.02763	0.001079	$7.127 \cdot 10^{-4}$	$2.093 \cdot 10^{-4}$	Menter SST
Q	0.03848	0.03307				RANS/LES

Table 7 Error assessment of the UMich. Mach 2.75, $\theta = 12.0$ deg case

Case	Error in					Turbulence model
	u/U_∞	v/U_∞	$\langle u^2 \rangle / U_\infty^2$	$\langle v^2 \rangle / U_\infty^2$	$\langle u'v' \rangle / U_\infty^2$	
Experiment	0.03473	0.008946	$6.092 \cdot 10^{-4}$	$1.585 \cdot 10^{-4}$	$1.551 \cdot 10^{-4}$	
B	0.04773	0.03172				Menter SST
G	0.04822	0.02965	0.001056	0.001095	$3.539 \cdot 10^{-4}$	Spalart-Allmaras
H	0.05748	0.04624	0.001378	0.001210	$5.538 \cdot 10^{-4}$	Menter BSL
M	0.04915	0.03348	0.001028	$9.323 \cdot 10^{-4}$	$2.920 \cdot 10^{-4}$	Menter SST
N	0.04258	0.02651	0.001195	$9.130 \cdot 10^{-4}$	$3.590 \cdot 10^{-4}$	Wilcox $k-\omega$ + Durbin correction
O	0.04176	0.02591	0.001193	$9.094 \cdot 10^{-4}$	$3.562 \cdot 10^{-4}$	Wilcox $k-\omega$
P	0.05064	0.03285	0.001169	$6.911 \cdot 10^{-4}$	$2.459 \cdot 10^{-4}$	Menter SST

normal stresses is important, scale-resolving methods should provide better accuracy.

3. Effect of Structured vs Unstructured Grids

Unstructured grid codes are widely used today. Table 4 denotes the grid type for each of the predictions for the IUSTI case. A similar spread in error levels is seen for both structured and unstructured methods, indicating that there is no discernible difference between the grid types.

4. Comparison with Hirsch's Findings

Hirsch compiled a "lessons learned" summary for the Chicago 2010 summer conference [4] based on the data presented at the January workshop. It must be noted that not all of the data presented at the workshop was submitted for this assessment; therefore, the information used for drawing conclusions is somewhat different. Hirsch based his comments on visual inspection of velocity profiles and contour plots comparing the various CFD solutions to the experiment. This is the traditional method for comparing data. It is worth examining how his findings compare with the findings based on the formal error assessment. Foremost, Hirsh stated, "it is remarkable that all the CFD results show similar and, at times, very close and highly consistent results. The scatter between different calculation results seems smaller than the deviations from experiments." This finding directly corresponds to the results of our formal assessment of the experimental and computational errors. Hirsch also concluded that there was no significant effect of the numerical scheme. This is also echoed by our results that show turbulence model dominance and the comparison of structured vs unstructured grids. Regarding turbulence models, Hirsch concluded that there was

"no clear dominant turbulence model," but he notes that the Wilcox $k-\omega$ and SST models show somewhat better trends followed by the SA model. We found that the Wilcox $k-\omega$ model was slightly superior to the SST model, then followed by the SA model.

V. Conclusions

A workshop on the CFD prediction of SBLIs was held at the 48th AIAA Aerospace Sciences Meeting in Orlando, Florida. As part of the workshop, numerous CFD analysts submitted solutions to four experimentally measured SBLIs. Assessments of both the measurements and predictions were performed to evaluate the current state of the art.

The experimental data for the four test cases came from two different sources: IUSTI in Marseilles, France, and UMich. A statistical uncertainty analysis of the UMich. data was performed and showed that the largest uncertainty was for the streamwise velocity and was (in the mean) 3.5% of the freestream velocity. The uncertainties in the turbulent Reynolds stresses were found to increase linearly with the magnitude of the stress.

An error metric that represents the average error in the predicted quantity for the entire data plane was defined and used to assess the relative quality of each of the submitted CFD solutions. It was found that the relative accuracy of the methods was not consistent between the variables of interest (i.e., a good prediction of u did not imply a good prediction of v or any other variable for a given method). Thus, the streamwise velocity was chosen to compare the computational methods. For the most part, the submitted solutions were remarkably similar in the error levels. The errors for all the solutions increased with increasing shock strength (increased deflection angle). The choice of turbulence model appears to be the dominant factor in the accuracy of the RANS solutions. Scale-resolving simulations had similar error levels as the RANS methods but provided superior predictions of the normal stresses. There appeared to be no dependence on computational grid type (structured or unstructured). These findings correspond very well to the summary of the workshop provided by Hirsch, who based his conclusions on a traditional examination of velocity profiles and contour plots [4].

The data show that there is a need for additional research in the prediction of SBLIs. First, high quality experimental data that

Table 8 Minimum and maximum error in streamwise velocity for the UMich. cases

Deflection angle, deg	Min. $E(u)/U_\infty$	Max. $E(u)/U_\infty$
7.75	0.02373	0.03995
10.0	0.03368	0.04584
12.0	0.04176	0.05748

include the effects of the sidewall and corner flow interactions is needed, and the uncertainty of the data should be quantified. RANS turbulence models that provide normal stresses, such as full Reynolds stress and algebraic Reynolds stress models, should be investigated for this problem. Finally, scale-resolving methods should continue to be advanced as they show promise for this type of flow.

Acknowledgments

The authors would like to thank all of those who contributed their solutions for this study. The significant time and effort that is represented by each solution is greatly appreciated. The authors would also like to thank the experimentalists who provided their data for the effort. In particular, Andrew Lapsa, Ethan Eagle, and Evan Bonny provided valuable insight that assisted in the uncertainty analysis of their experiments at the University of Michigan.

References

- [1] Delery, J., and Marvin, J. G., "Shock-Wave Boundary Layer Interactions," edited by E. Reshotko, AGARD No. 280, 1986.
- [2] Benek, J., "Overview of the 2010 AIAA Shock Boundary Layer Interaction Workshop," *28th AIAA Applied Aerodynamics Conference*, AIAA Paper 2010-4821, Chicago, IL, 2010.
- [3] Benek, J., and Babinsky, H., "Lessons Learned from the 2010 AIAA Shock Boundary Layer Interaction Workshop," *28th AIAA Applied Aerodynamics Conference*, AIAA Paper 2010-4825, Chicago, IL, 2010.
- [4] Hirsch, C., "SBLI Lessons Learned: CFD Simulations of Two Test Cases," *28th AIAA Applied Aerodynamics Conference*, AIAA Paper 2010-4824, Chicago, IL, 2010.
- [5] DeBonis, J. R., Oberkampf, W. L., Wolf, R. T., Orkwis, P. D., and Turner, M. G., "Assessment of CFD Models for Shock Boundary—Layer Interaction," *28th AIAA Applied Aerodynamics Conference*, AIAA Paper 2010-4823, Chicago, IL, 2010.
- [6] Dupont, P., Piponnaiu, S., Sidorenko, A., and Debieve, J., "Investigation by Particle Image Velocimetry Measurements of Oblique Shock Reflection with Separation," *AIAA Journal*, Vol. 46, No. 6, 2008, pp. 1365–1370.
doi:10.2514/1.30154
- [7] Lapsa, A. P., "Experimental Study of Passive Ramps for Control of ShockBoundary Layer Interactions," Ph.D. Thesis, The Univ. of Michigan, Ann Arbor, MI, 2009.
- [8] Lapsa, A. P., and Dahm, W. J. A., "Stereo Particle Image Velocimetry of Nonequilibrium Turbulence Relaxation in a Supersonic Boundary Layer," *Experiments in Fluids*, Vol. 50, No. 1, 2011, pp. 89–108.
doi:10.1007/s00348-010-0897-x
- [9] Oberkampf, W. L., and Aeschliman, D. P., "Joint Computational/Experimental Aerodynamics Research on a Hypersonic Vehicle: Part 1, Experimental Results," *AIAA Journal*, Vol. 30, No. 8, 1992, pp. 2000–2009.
- [10] Oberkampf, W. L., Aeschliman, D. P., Henfling, J. F., and Larson, D. E., "Surface Pressure Measurements for CFD Code Validation in Hypersonic Flow," *26th Fluid Dynamics Conference*, AIAA Paper 1995-2273, San Diego, CA, 1995.
- [11] Oberkampf, W. L., and Roy, C. J., *Verification and Validation in Scientific Computing*, Cambridge Univ. Press, Cambridge, England, UK, 2010.
- [12] Dussauge, J. P., Debieve, J. F., Dupont, P., Piponnaiu, S., and Souverein, L. J., "Final Report on the Measurements of Shock Reflection at $M = 2.25$," UFAST, IUSTI Deliverable No. 3.3.5, 2009.
- [13] Montgomery, D. C., *Design and Analysis of Experiments*, 5th ed., Wiley, New York, 2000.
- [14] Montgomery, D. C., *Statistics for Experimenters: Design, Innovation, and Discovery*, 2nd ed., Wiley, Hoboken, NJ, 2005.
- [15] Coleman, H. W., and Steele, W. G., Jr., *Experimentation and Uncertainty Analysis for Engineers*, 2nd ed., Wiley, New York, 1999.
- [16] Menter, F. R., "Two-Equation Eddy-Viscosity Turbulence Models for Engineering Applications," *AIAA Journal*, Vol. 32, No. 8, 1994, pp. 1598–1605.
doi:10.2514/3.12149
- [17] Wilcox, D. C., *Turbulence Modeling for CFD*, 2nd ed., DCW Industries, La Cañada, CA, 1998.
- [18] Durbin, P. A., "On the $k-\epsilon$ Stagnation Point Anomaly," *International Journal of Heat and Fluid Flow*, Vol. 17, 1996, pp. 89–90.
doi:10.1016/0142-727X(95)00073-Y
- [19] Shih, T.-H., Liou, W. W., Shabbir, A., Yang, Z., and Zhu, J., "A New $k-\epsilon$ Eddy Viscosity Model for High Reynolds Number Turbulent Flows," *Computers and Fluids*, Vol. 24, No. 3, 1995, pp. 227–238.
doi:10.1016/0045-7930(94)00032-T
- [20] Spalart, P. R., and Allmaras, S. R., "A One-Equation Turbulence Model for Aerodynamic Flows," *Recherche Aerospatiale*, No. 1, 1994, pp. 5–21.
- [21] Gieseking, D. A., Choi, J.-I., Edwards, J. R., and Hassan, H. A., "Simulation of Shock/Boundary Layer Interactions Using Improved LES/RANS Models," *48th AIAA Aerospace Sciences Meeting*, AIAA Paper 2010-111, Orlando, FL, 2010.
- [22] Jaberi, F. A., Colucci, P. J., James, S., Givi, P., and Pope, S. B., "Filtered Mass Density Function for Large-Eddy Simulation of Turbulent Reacting Flows," *Journal of Fluid Mechanics*, Vol. 401, 1999, pp. 85–121.
doi:10.1017/S0022112099006643
- [23] Park, M. A., and Carlson, J.-R., "Turbulent Output-Based Anisotropic Adaptation," *48th AIAA Aerospace Sciences Meeting*, AIAA Paper 2010-168, Orlando, FL, 2010.
- [24] Pirozzoli, S., and Grasso, F., "Direct Numerical Simulation of Impinging Shock Wave/Turbulent Boundary Layer Interaction at $M = 2.25$," *Physics of Fluids*, Vol. 18, No. 6, 2006, pp. 065113-1–065113-17.
doi:10.1016/j.ijheatfluidflow.2008.07.001
- [25] Shur, M. L., Spalart, P. R., Strelets, M. K., and Travin, A. K., "A Hybrid RANS-LES Approach with Delayed-DES and Wall-Modeled LES Capabilities," *International Journal of Heat and Fluid Flow*, Vol. 29, 2008, pp. 1638–1649.
doi:10.1016/j.ijheatfluidflow.2008.07.001
- [26] Launder, B. E., and Sharma, B. I., "Application of the Energy Dissipation Model of Turbulence to the Calculation of Flow Near a Spinning Disc," *Letters in Heat and Mass Transfer*, Vol. 1, No. 2, 1974, pp. 131–138.
doi:10.1016/0094-4548(74)90150-7
- [27] Georgiadis, N. J., Rumsey, C. L., Yoder, D. A., and Zaman, K. B. M. Q., "Turbulence Modeling Effects on Calculation of Lobed Nozzle Flowfields," *Journal of Propulsion and Power*, Vol. 22, No. 3, 2006, pp. 567–575.
doi:10.2514/1.17160

D. Gaitonde
Associate Editor